Multiparametric MRI analysis for the evaluation of MR-guided high intensity focused ultrasound tumor treatment

Multiparametric MRI analysis for the evaluation of MR-guided high intensity focused ultrasound tumor treatment

Stefanie J. C. G. Hectors[a,b†], Igor Jacobs[a†], Edwin Heijman[c], Jochen Keupp[d], Monique Berben[c], Gustav J. Strijkers[a,e], Holger Grüll[a,c] and Klaas Nicolay[a]*

For the clinical application of high intensity focused ultrasound (HIFU) for thermal ablation of malignant tumors, accurate treatment evaluation is of key importance. In this study, we have employed a multiparametric MRI protocol, consisting of quantitative T_1, T_2, ADC, amide proton transfer (APT), $T_{1\rho}$ and DCE-MRI measurements, to evaluate MR-guided HIFU treatment of subcutaneous tumors in rats. K-means clustering using all different combinations of the endogenous contrast MRI parameters (feature vectors) was performed to segment the multiparametric data into tissue populations with similar MR parameter values. The optimal feature vector for identification of the extent of non-viable tumor tissue after HIFU treatment was determined by quantitative comparison between clustering-derived and histology-derived non-viable tumor fractions. The highest one-to-one correspondence between these clustering-based and histology-based non-viable tumor fractions was observed for the feature vector {ADC, APT-weighted signal} (R^2 to line of identity ($R^2_{y=x}$) = 0.92) and the strongest agreement was seen 3 days after HIFU ($R^2_{y=x}$ = 0.97). To compare the multiparametric MRI analysis results with conventional HIFU monitoring and evaluation methods, the histology-derived non-viable tumor fractions were also quantitatively compared with non-perfused tumor fractions (derived from the level of contrast enhancement in the DCE-MRI measurements) and 240 CEM tumor fractions (i.e. thermal dose > 240 cumulative equivalent minutes at 43 °C). The correlation between histology-derived non-viable tumor fractions directly after HIFU and the 240 CEM fractions was high, but not significant. The non-perfused fractions overestimated the extent of non-viable tumor tissue directly after HIFU, whereas an underestimation was observed 3 days after HIFU.

In conclusion, we have shown that a multiparametric MR analysis, especially based on the ADC and the APT-weighted signal, can potentially be used to determine the extent of non-viable tumor tissue 3 days after HIFU treatment. We expect that this method can be incorporated in the current clinical workflow of MR–HIFU ablation therapies. Copyright © 2015 John Wiley & Sons, Ltd.

Additional supporting information may be found in the online version of this article at the publisher's web site.

Keywords: high intensity focused ultrasound; multiparametric MRI; cluster analysis; treatment response; cancer

INTRODUCTION

High intensity focused ultrasound (HIFU) is a promising technique for the non-invasive thermal treatment of tumors (1,2). For the clinical introduction of HIFU for thermal ablation of malignant tumors, accurate treatment planning, monitoring and therapy assessment are of critical importance to ensure a successful and safe treatment. To fulfill these needs, HIFU treatment is generally performed under image guidance, using either MRI or ultrasound. In an MR-guided HIFU (MR–HIFU) system, the HIFU transducer is, e.g., integrated in the patient bed of a clinical MR scanner. MR thermometry can be utilized to monitor the temperature evolution in real time (3), allowing for the definition

* Correspondence to: K. Nicolay, Biomedical NMR, Department of Biomedical Engineering, Eindhoven University of Technology, Eindhoven, The Netherlands.
E-mail: k.nicolay@tue.nl

a S. J. C. G. Hectors, I. Jacobs, G. J. Strijkers, H. Grüll, K. Nicolay
Biomedical NMR, Department of Biomedical Engineering, Eindhoven University of Technology, Eindhoven, The Netherlands

b S. J. C. G. Hectors
Translational and Molecular Imaging Institute, Icahn School of Medicine at Mount Sinai, New York, USA

c E. Heijman, M. Berben, H. Grüll
Oncology Solutions, Philips Research Europe, Eindhoven, The Netherlands

d J. Keupp
Tomographic Imaging Systems, Philips Research Europe, Hamburg, Germany

e G. J. Strijkers
Biomedical Engineering and Physics, Academic Medical Center, University of Amsterdam, Amsterdam, The Netherlands

† These authors contributed equally.

of thermal dose areas that are lethal to the tumor tissue (i.e. tumor regions in which the delivered thermal dose was at least 240 cumulative equivalent minutes (CEM) at 43 °C) (4,5). In addition, the excellent soft tissue contrast of MRI offers unique possibilities for treatment planning and evaluation.

Clinical evaluation of HIFU treatment with MRI has been mainly restricted to T_2-weighted and contrast-enhanced T_1-weighted imaging. Although these methods provide useful information about treatment response (6–10), they often lack the sensitivity and/or specificity to accurately identify the non-viable tumor tissue after HIFU (10–12).

We have previously shown that HIFU-treated non-viable tumor tissue can be accurately identified 3 days after HIFU treatment using a multiparametric MRI analysis of combined T_1, T_2 and apparent diffusion coefficient (ADC) data (13). However, directly after treatment, the multiparametric analysis performed less well with respect to the identification of non-viable tumor tissue. Other MRI methods, especially those that are sensitive to protein denaturation and aggregation, which occur instantly during HIFU treatment, may be more suitable for direct treatment evaluation. Amide proton transfer (APT) imaging is a very promising method for tumor tissue characterization (14–19) and treatment evaluation (20). APT imaging selectively measures the saturation transfer from amide protons of mobile proteins and peptides to bulk water protons. Another MR parameter that is sensitive to macromolecular changes in the tumor tissue is the longitudinal relaxation time in the rotating frame ($T_{1\rho}$). $T_{1\rho}$ is primarily sensitive to protein–water interactions. In recent studies we have shown that APT imaging and $T_{1\rho}$ mapping are both promising MRI methods for the detection of HIFU-induced macromolecular tissue changes (21,22).

We hypothesized that inclusion of these advanced MR contrast parameters in the previously described multiparametric analysis leads to a more accurate identification of successfully HIFU-treated tumor tissue. Therefore, the goal of the current study was to identify a subset of MRI parameters that are suitable for accurate early HIFU therapy assessment. In addition, we aimed to compare the performance of this optimal multiparametric analysis with conventional HIFU monitoring and evaluation methods, namely MR thermometry and contrast-enhanced MRI. Such quantitative comparison with conventional techniques could not be performed in our previous studies (13,21,22), mainly because the HIFU treatment was performed outside the MR system. In the present study, the HIFU treatment was performed in a rat tumor model on a clinical 3 T MR–HIFU system, allowing for real-time acquisition of MR temperature maps during treatment. The multiparametric MRI protocol, consisting of quantitative T_1, T_2, ADC, APT and $T_{1\rho}$ mapping, was performed in the same MR–HIFU system before, directly after and 3 days after HIFU treatment. In addition, dynamic contrast-enhanced MRI (DCE-MRI) was performed after HIFU to assess changes in the tumor vascular status and to determine the non-perfused tumor volume after treatment. Cluster analysis, which segments the multiparametric data into tissue populations with similar MR parameter values, was performed on all possible combinations of the endogenous MR contrast parameters. The optimal subset of MRI parameters for HIFU treatment evaluation was determined by quantitative comparison between clustering-derived and histology-derived non-viable tumor fractions. The performance of the proposed multiparametric analysis with respect to the identification of non-viable tumor tissue was compared with contrast-enhanced MRI and MR thermometry by quantitative correlation analyses between clustering-derived non-viable tumor fractions, non-perfused tumor fractions, 240 CEM tumor fractions (i.e. the fraction of the tumor in which the thermal dose exceeded 240 CEM) and histology-derived non-viable tumor fractions.

EXPERIMENT

Ethics statement

All animal experiments were performed according to Directive 2010/63/EU of the European Commission and approved by the Animal Care and Use Committee of Maastricht University (protocol 2012–171).

Rat tumor model

Five- to seven-week-old female Fischer 344 rats (Charles River, Maastricht, The Netherlands) were inoculated with 1×10^6 GS 9L cells (early passages of the original batch obtained from Public Health England, London, UK) in 100 µL phosphate buffered saline (Sigma-Aldrich, St Louis, MO, USA), subcutaneously in the left hind limb. The average tumor size at the time of the first MRI examination was 878 ± 533 mm^3 as determined from region-of-interest (ROI) analysis on the anatomical MR images.

Study design

The tumor-bearing rats underwent MRI directly before ($n = 12$), directly after ($n = 12$) and 3 days after ($n = 6$) HIFU treatment. A non-treated control group ($n = 6$) was included that underwent MRI at the same time points, but did not undergo MR–HIFU treatment. Immediately after the final MRI measurement, rats were sacrificed by cervical dislocation and tumors were excised for histological analysis. This study design resulted in three different groups for histology: rats that were sacrificed immediately after the MRI scan directly after MR–HIFU ablation (referred to as 'directly after HIFU', $n = 6$), rats that were sacrificed directly after the MRI scan 3 days after MR–HIFU ablation (referred to as '3 days after HIFU', $n = 6$) and a non-treated control group (referred to as 'control', $n = 6$).

MR-guided HIFU treatment

MR–HIFU system and small animal set-up

HIFU treatment was performed using a clinical 3 T MR–HIFU system (Philips Sonalleve, Philips Healthcare, Vantaa, Finland). A dedicated small animal HIFU-compatible MR receiver coil (Philips Healthcare, Vantaa, Finland) with a multi-channel volumetric design was used to obtain optimal signal to noise ratio. The utilized MR–HIFU system and small animal set-up have been described in detail previously (23).

Animal handling

Animals were anesthetized with 3% isoflurane in medical air (0.6 L/min) and maintained with 1.0–2.5% isoflurane during the HIFU treatment and MRI measurements. At least 30 min prior to HIFU treatment, precautionary analgesia was given (carprofen; Rimadyl, 4 mg/kg s.c.). An equal dose of analgesia was administered to the control animals before the first MRI measurement. For optimal coupling of the ultrasound to the skin, fur was removed from the tumor and hind limb by shaving and application of a

depilatory cream (Veet, Hoofddorp, The Netherlands). During MRI measurements and MR–HIFU treatment, the animal's respiration rate was monitored with a pressure balloon sensor (Graseby, Smiths Medical, St Paul, MN, USA) and core body temperature was monitored using a rectal optical temperature probe (Neoptix, Quebec City, Canada) and maintained at 37 °C using a custom-made warm water circuit with temperature feedback. The tumor-bearing paw was submerged in a mixture of degassed ultrasound gel and water. Similar to regulation of the animal's temperature, the temperature of the gel–water mixture was monitored and maintained at 37 °C using an optical temperature probe and a warm water circuit. More specific details of the MR–HIFU system used can be found elsewhere (23).

HIFU treatment

A 4 mm diameter treatment cell was positioned within the tumor using anatomical MR images. Volumetric thermal ablation of the tumor tissue was performed with a 256-element spherical phased array transducer (aperture = 13 cm, focal length = 12 cm, ellipsoid focal spot size (-6 dB) = $1 \times 1 \times 7$ mm^3). A single focus point was electronically steered along a circular trajectory, consisting of eight points (50 ms sonication time/point), perpendicular to the direction of ultrasound propagation, as described previously (23,24). The order of sonication was chosen in such a way that the distance between successive points was maximized, ensuring an even temperature rise over the entire circle. Ultrasound was applied as a continuous wave with a frequency of 1.44 MHz. Thermal ablation was performed by 90 s sonication at 35 W acoustic power (resulting in an average maximum ablation temperature of 58.5 ± 5.6 °C ($n = 12$)). The sonication time was intentionally kept constant rather than using the MR thermometry-based feedback control to stop the sonication when a certain target temperature or thermal dose was reached. It has been previously described that HIFU treatment using a constant power and sonication time without feedback results in a wider spread of temperatures in the treatment volume and subsequently in a larger variation in the thermal lesion size, as compared with sonications with MR thermometry feedback (25). Since a large spread in thermal lesion size and subsequently a large range of non-viable tumor fractions was beneficial for the correlation analyses between MRI-derived and histology-derived non-viable tumor fractions in the current study, the sonications were performed without thermometry feedback. Tumors were only partially treated with a single treatment cell, which was smaller than the typical tumor diameter, to allow for the presence of both treated and untreated tumor tissue in the multiparametric MR images.

MRI protocol

The MRI protocol started with a T_2*-weighted 3D gradient-echo acquisition ($T_R = 15$ ms, $T_E = 12$ ms, field of view (FOV) = $280 \times 280 \times 20$ mm^3, acquisition matrix = $256 \times 256 \times 10$, reconstruction matrix = $1008 \times 1008 \times 10$, reconstructed voxel size = $0.28 \times 0.28 \times 2$ mm^3, flip angle (FA) = 10°, number of averages (NA) = 2, scan duration = 1 min 58 s) to check for the presence of air bubbles in the HIFU beam path or in close proximity to the tumor tissue. A relatively large FOV was chosen for this sequence in order to visualize the entire water–gel mixture surrounding the tumor-bearing paw.

The HIFU treatment cell was planned on anatomical images covering the entire tumor, acquired with a multi-slice steady-state gradient-echo sequence ($T_R = 793$ ms, $T_E = 13$ ms, FOV = $40 \times 48 \times 20$ mm^3, acquisition and reconstruction matrix = $160 \times 192 \times 20$, reconstructed voxel size = $0.25 \times 0.25 \times 1$ mm^3, FA = 20°, NA = 2, scan duration = 5 min 6 s).

The temperature rise in the treatment area during MR–HIFU ablation was monitored with a dynamic gradient-echo segmented echo planar imaging (EPI) acquisition ($T_R = 38$ ms, $T_E = 20$ ms, FOV = 250×250 mm^2, acquisition matrix = 176×169, reconstruction matrix = 176×176, reconstructed voxel size = $1.42 \times 1.42 \times 4.08$ mm^3, FA = 19.5°, EPI factor = 7, NA = 2, temporal resolution = 4.8 s) in three adjacent slices perpendicular and one slice parallel to the acoustic beam path.

The multiparametric MRI protocol consisted of quantitative assessment of the T_1, T_2, ADC, APT-weighted signal and $T_{1\rho}$ as well as a DCE-MRI acquisition. For the HIFU-treated animals, DCE-MRI was only performed after the HIFU treatment, since the presence of the paramagnetic Gd could affect the assessment of the endogenous contrast parameters directly after treatment and induce inaccuracies in the temperature mapping due to magnetic susceptibility changes (26). The multiparametric acquisitions performed directly after treatment were started after the temperature of the tumor-bearing paw was decreased to baseline temperature again (5–10 min waiting time) to prevent influences of temperature changes on the MRI parameter estimations. The orientation of the central slice of all imaging methods of the multiparametric MRI protocol was aligned with the central slice of the temperature mapping sequence, perpendicular to the acoustic beam axis. Acquisition details for the multiparametric protocol are given in Table 1. For the DCE-MRI sequence the number of slices was increased to 15, as opposed to five in the rest of the multiparametric protocol, in order to avoid aliasing artifacts, with the same center slice positions and reconstructed voxel size as for the other sequences.

The total acquisition time of the multi-slice multiparametric protocol was approximately 75 min.

Image processing and generation of parameter maps

Data analysis was performed with Mathematica 8.0 (Wolfram Research, Champaign, IL, USA) and MATLAB R2013a (MathWorks, Natick, MA, USA). Tumor ROIs were manually drawn using the image with $T_E = 37.1$ ms of the T_2 mapping dataset. Diffusion-weighted images were used as a visual reference for the correct identification of tumor tissue. Parameter maps were calculated on a pixel-by-pixel basis in each slice. Only the central slice of the multiparametric images was selected for all further analyses, since the orientation of this slice corresponded to the central slice of the temperature maps perpendicular to the HIFU beam axis. T_1 maps were generated as described previously (27). To calculate the T_2 maps, mono-exponential fitting was performed through the multi-echo data, omitting the first two echoes due to signal fluctuations. The ADC was determined by mono-exponential fitting through the signal intensities at the four highest b values (400, 600, 800, 1200 s/mm^2).

For analysis of the APT data, first the minimum of the z-spectrum was determined by fitting a 23rd-order polynomial function through the z-spectrum, after which the minimum of this function was calculated. An example of a fitted z-spectrum curve can be found in the Supplementary Information (Fig. S1). Subsequently, the minimum of the z-spectrum was centered at

Table 1. Acquisition details of the multiparametric MRI protocol

	T_1 mapping	T_2 mapping	ADC mapping	APT imaging	$T_{1\rho}$	DCE-MRI
Sequence type	3D Look–Locker segmented gradient echo	2D fast spin echo	2D diffusion-weighted EPI	3D turbo gradient echo	3D gradient echo	3D RF-spoiled turbo gradient echo
T_E [ms]	2.8	4.1–251.7 (16.5ms steps)	71	3.8	2.1	2.6
T_R [ms]	5.6	14 526	1000	7.5	3.6	5.2
FA [°]	5	90/180	90/180	20	20	15
Number of slices	5	5	5	5	5	15
Slice thickness [mm]	2	2	2	2	2	2
FOV [mm²]	150 × 150	150 × 150	150 × 150	150 × 150	150 × 150	150 × 150
Image matrix	160 × 160	160 × 160	160 × 160	160 × 160	160 × 160	160 × 160
NA	1	1	2	2	8	1
Sequence-specific details	T_I range 18–6418 ms (100 ms steps); turbo factor 10	–	b values 0, 100, 200, 400, 600, 800, 1200 s/mm²; EPI factor 11	saturation pulse frequency offsets −6 to 6 ppm (0.5 ppm steps) and ~−1560 ppm(control S_0 acquisition), duration 2 s, saturation amplitude 1.8 µT; turbo factor 75; local second-order pencil beam shim	spin-lock preparation compensated for B_1 and B_0 field imperfections (51); spin-lock durations 5 and 40 ms; spin-lock amplitude 350 Hz	temporal resolution 4.3 s, CA (0.2 mmol/kg Gd-DOTA/Dotarem; Guerbet, Villepente, France) injection 1 min after start of acquisition with infusion pump (5 s infusion at 3 mL/min; Chemyx Fusion 100; Stafford, TX, USA)
Scan duration	8 min	12 min 35 s	9 min 22 s	17 min 50 s	3 min 54 s	10 min 46 s

0 ppm and the APT-weighted signal maps were generated via a magnetization transfer asymmetry (MTR_{asym}) analysis using $MTR_{asym} = (S_{sat}(-3.5\ ppm) - S_{sat}(3.5\ ppm))/S_0$, in which $S_{sat}(-3.5\ ppm)$ and $S_{sat}(3.5\ ppm)$ are the signal intensities in the z-spectrum at -3.5 ppm and 3.5 ppm from the water frequency, respectively, and S_0 is the signal intensity in the acquisition with the saturation offset far from the water peak (~ -1560 ppm). The $T_{1\rho}$ values were determined by calculation of $(t_{sl,2} - t_{sl,1})/\ln(SI_{sl,1}/SI_{sl,2})$, where $t_{sl,1}$ and $t_{sl,2}$ are the different spin-lock durations and $SI_{sl,1}$ and $SI_{sl,2}$ are the corresponding signal intensities.

From the DCE-MRI data, dynamic T_1 values were calculated in the tumor ROIs from the dynamic signal intensities and the pre-contrast T_1 values using the signal equation for an RF-spoiled gradient-echo sequence (28). Dynamic T_1 values were converted to dynamic contrast agent concentrations ([CA]) using the relaxivity of Dotarem (3.78 mM^{-1} s^{-1}), which was measured *ex vivo* in rat plasma at 3 T at 37 °C. Tracer-kinetic analysis of the DCE-MRI data was performed with a custom-written MATLAB tool. The standard Tofts model (29) was fitted to the DCE-MRI data to determine the transfer constant K^{trans} and extravascular extracellular volume fraction v_e in each tumor pixel. A delay term (t_d) was included in the model to allow for a delay between bolus arrival in the blood and the tissue response. A population-averaged bi-exponential arterial input function (AIF) was used as proposed by McGrath *et al*. (30). The bi-exponential AIF is described by

$$C\rho(t) = \begin{cases} 0 & t < t_i \\ a_1 e^{-m_1 t} + a_2 e^{-m_2 t} & t \geq t_i \end{cases}$$

in which t_i is the injection time. The exponents of the bi-exponential function were determined based on blood kinetics data of Dotarem acquired in three separate female Fischer 344 rats. Blood sampling in these separate animals was performed from the saphenous vein at different time points (0.5, 2, 5, 10, 15, 20, 30 min) after CA injection. The Gd^{3+} concentration in the blood samples was determined by means of inductively coupled plasma–atomic emission spectrometry or inductively coupled plasma–mass spectrometry. The blood concentrations of Gd^{3+} were converted to plasma concentrations using a hematocrit value of 53.8% as reported for the rat strain used (31). Subsequently, the bi-exponential model was fitted to the time–plasma concentration data points. The a_1 and a_2 parameters following from this fit were adapted such that the sum of a_1 and a_2 was equal to the theoretical peak concentration, which was calculated based on the injected dose and the rat plasma volume. These adaptations led to the following bi-exponential AIF parameters: $a_1 = 5.38$ mM, $a_2 = 1.38$ mM, $m_1 = 2.82$ min^{-1}, $m_2 = 0.04$ min^{-1}.

The standard Tofts model was fitted to the dynamic [CA] curves using the MATLAB function lsqcurvefit, with constraints $K^{trans} \geq 0$ min^{-1}, k_{ep} ($=K^{trans}/v_e$) ≥ 0 min^{-1} and $0 \leq t_d \leq 7$ repetitions. Tumor pixels were considered non-perfused if the median dynamic [CA] after injection was less than five times the standard deviation (SD) of the data points in the dynamic [CA] curve before injection.

Maximum temperature maps were generated from the acquired MR thermometry data. Thermal dose maps were calculated using the Sapareto–Dewey equation (32) with 43 °C as reference temperature. Although the slice orientation was the same for the temperature maps and the multiparametric MR images, the image resolution and position within the slice plane of the temperature maps and multiparametric MR images were different. Therefore, registration of the temperature maps to the multiparametric images was performed by translation and interpolation of the temperature maps in the slice plane. 240 CEM thermal dose areas were defined and MR parameter changes directly after MR–HIFU treatment were related to the maximum temperature and thermal dose.

Histograms of the parameter values in the tumor pixels at the different time points were calculated for all MRI parameters to assess HIFU-induced changes in the parameter distributions.

Cluster analysis

k-means cluster analysis was performed to segment the multiparametric MRI data into groups of pixels, i.e. clusters, with similar MR parameter values (33). Clustering was performed on all data (i.e. of all animals (both treated and non-treated) and all time points) simultaneously. Prior to clustering, the parameter values were normalized (mean = 0, SD = 1) to prevent scaling bias between the different MR parameters. Clustering was performed with a custom-written Mathematica tool with two to six clusters and all possible feature vectors (i.e. all different combinations of MR parameters). The pharmacokinetic parameters resulting from the DCE-MRI analysis were not included in the cluster analysis, since DCE-MRI was only performed after treatment.

After clustering with the different feature vectors, clusters were defined as non-viable if the fraction of pixels that was assigned to that cluster significantly increased after MR–HIFU ablation (either directly or 3 days after ablation) compared with before treatment (one-sided paired Student's *t* test, $P < 0.05$). The remaining clusters were defined as viable. Subsequently, all tumor pixels were classified as either viable or non-viable based on the cluster to which they were assigned. Based on this classification, the *k*-means clustering-derived non-viable tumor fractions were calculated for each tumor and for each feature vector.

Histology

After sacrifice, the skin was removed from the tumor and four lines of different colors were drawn on the tumor tissue using a tissue-marking dye kit (Sigma-Aldrich). The planes in which the lines were applied were perpendicular to the direction of the MRI slices, which was retrieved by using the acquired anatomical MRI images as a visual reference. The exact positioning of the four lines can be observed in the Supplementary Information (Fig. S2). Subsequently, the entire tumor was removed and put in a dedicated tissue holder. Using the applied color lines and the MRI images as reference, the tumor was cut into two pieces, such that the cutting face matched with the central slice of the multiparametric and MR thermometry acquisitions. Subsequently, one of the pieces was processed to prepare paraffin sections and the other to prepare cryosections. For cryosections, tumors were embedded in Cryomatrix (Shandon, Thermo Scientific, Waltham, MA, USA), snap-frozen in isopentane at -40 °C and stored at -80 °C. For paraffin sections, the tumors were fixed in 4% formaldehyde solution for approximately 40 h and then stored in 70% ethanol until they were embedded in paraffin. Both the paraffin-embedded and the snap-frozen tumor pieces were subsequently cut into 5–6 μm thick sections.

For quantitative assessment of the non-viable tumor fraction, cryosections were briefly air-dried and subsequently stained for

nicotinamide adenine dinucleotide (NADH) diaphorase activity as a marker for cell viability. Tumor sections were incubated in filtered Gomori Tris–HCl buffer at pH 7.4, with 0.71 mg/mL β-NAD reduced disodium salt hydrate (Sigma-Aldrich) and 0.29 mg/mL nitro blue tetrazolium (Sigma-Aldrich) for 1 h at 37 °C.

The paraffin sections were used for hematoxylin and eosin (H&E; Sigma-Aldrich) staining to assess morphological tumor changes after MR–HIFU ablation.

After staining, one paraffin section and one cryosection were selected (blinded from the MRI results) for each tumor and brightfield microscopy was performed on a Pannoramic MIDI digital slide scanner (3DHistech Ltd, Budapest, Hungary) at 41× magnification to obtain images of the entire tumor section.

Analysis of the microscopy images of the NADH diaphorase-stained tumor sections was performed in Mathematica 8.0. For quantification of the non-viable tumor fraction, ROIs were
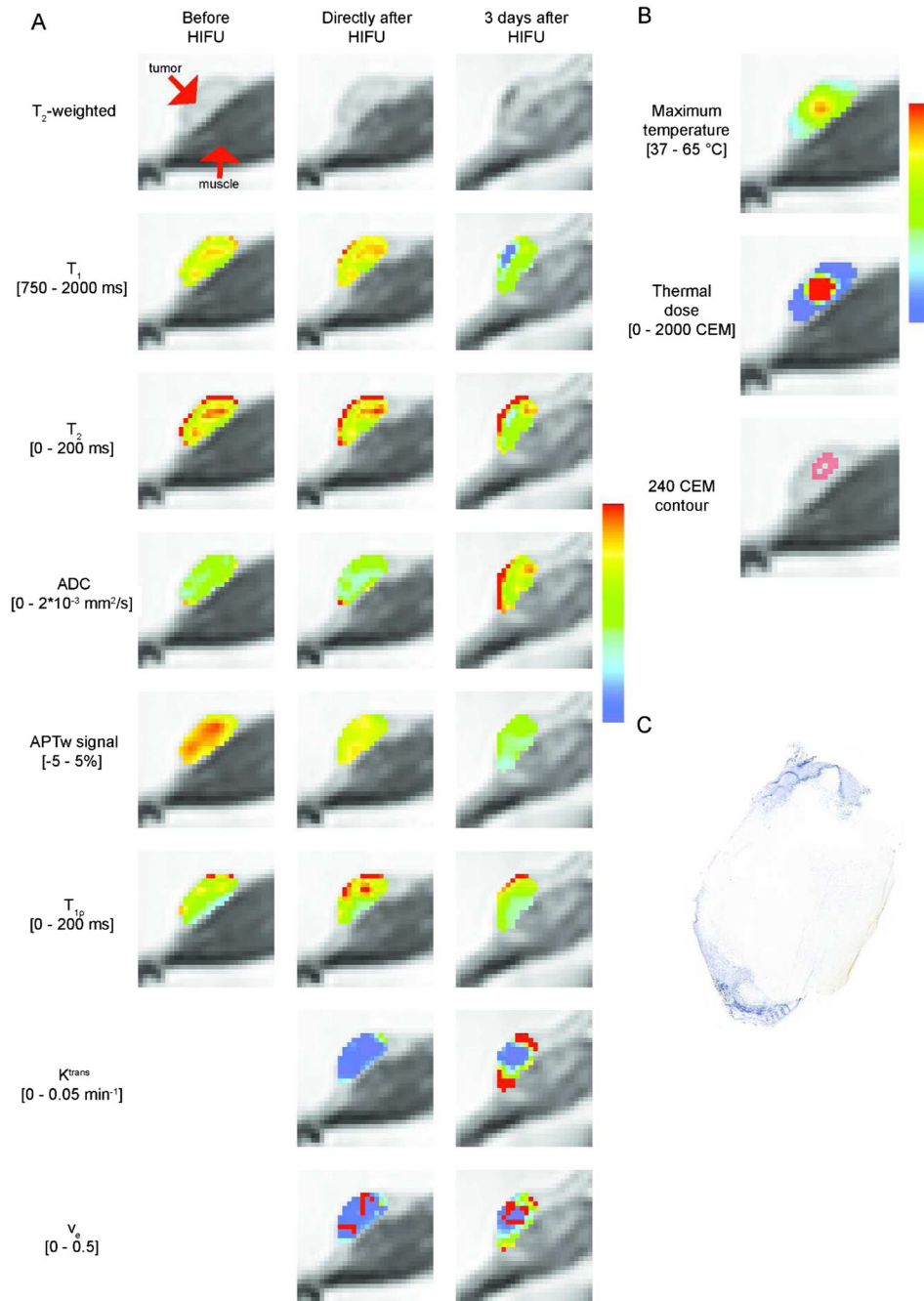
Figure 1. (A) Representative T_2-weighted images and MR parameter maps (T_1, T_2, ADC, APTw signal, $T_{1\rho}$, K^{trans} and v_e) superimposed on the T_2-weighted images in the center slice of the tumor-bearing hind limb, before, directly after and 3 days after HIFU treatment. The parameter maps of K^{trans} and v_e before HIFU are absent, since DCE-MRI was not performed at this time point. The color coding represents the MR parameter values in the tumor, of which the scaling is given by the scale bar on the right and the range is indicated on the left of each row. (B) Maps of the maximum temperature that was reached (top) and the applied thermal dose in each tumor pixel (bottom). The scale bar on the right and the numbers on the left represent the range in parameter values. (C) The NADH diaphorase-stained tumor section at the same location as the shown MRI slice, excised 3 days after HIFU treatment. The blue region is viable tumor and the pale region is non-viable tumor.

manually drawn around the entire tumor tissue and around the pale non-viable tumor tissue. For each tumor the non-viable tumor fraction was determined from the ratio between the two ROI areas.

Comparison between MRI and histology

The cluster results of the different feature vectors were analyzed by quantitative comparison between clustering-derived and histology-derived non-viable tumor fractions. This comparison was done by assessment of the Pearson's correlation coefficient and the one-to-one correspondence between the fractions. The latter was determined by calculation of the coefficient of determination ($R^2_{y=x}$) between the data points and the line of identity. $R^2_{y=x}$ was calculated using the following formula (34):

$$R^2_{y=x} = 1 - \frac{\sum (y_i - x_i)^2}{\sum y_i^2},$$

in which x_i and y_i are the non-viable fractions derived from histology and clustering, respectively. All groups ('directly after HIFU', '3 days after HIFU' and 'control') were combined in this analysis. The feature vector with the highest one-to-one correspondence between clustering-derived and histology-derived non-viable tumor fractions was selected as the optimal feature vector for the identification of non-viable tumor tissue. After selection of the optimal feature vector, the one-to-one correspondence and Pearson's correlation coefficient between clustering-derived non-viable tumor fractions and histology-derived non-viable tumor fractions were also determined separately for the different experimental groups. The histology-derived non-viable fractions were also quantitatively compared with the DCE-MRI-derived non-perfused fractions and the 240 CEM fractions, again by calculation of $R^2_{y=x}$ and the correlation coefficient.

Statistical analysis

All data are shown as mean ± SD. Two-sided paired t-tests were used to compare the average parameter values in the tumor ROI at both time points after HIFU treatment with before treatment, the histograms of the endogenous contrast MRI parameters at both time points after HIFU treatment with before treatment, and the average parameter values in the 240 CEM area before and directly after HIFU ablation. Two-sided t-tests assuming equal variances were used to compare the average pharmacokinetic parameter values in the HIFU-treated and non-treated control tumors at the corresponding timepoints, and the K^{trans} and v_e histograms of the HIFU-treated and non-treated control animals at corresponding time points. The calculated Pearson's correlation coefficients were tested for significance with a one-sample t-test. For all tests, the level of significance was set to $\alpha = 0.05$.

RESULTS

MR parameter maps and average parameter values

Representative MR parameter maps at the different experimental time points ('before HIFU', 'directly after HIFU' and '3 days after HIFU') are shown in Fig. 1(A). The observed changes in the individual endogenous MR parameter values after HIFU treatment were rather subtle and heterogeneous between the different endogenous contrast parameters. The K^{trans} maps derived from the DCE-MRI measurements showed that the tumor was largely non-perfused directly after treatment, while the perfusion was partly restored 3 days after treatment. On the maximum temperature maps (Fig. 1(B)) a circular region was observed in which a significant temperature increase was measured. This circular region was more distinctly visible on the thermal dose maps (Fig. 1(B)), because of the exponential increase of thermal dose at higher temperatures. The NADH-diaphorase-stained tumor section shown in Fig. 1(C), obtained at approximately the same position and orientation in the tumor as the MRI slice 3 days after HIFU treatment, shows mostly non-viable tumor (pale) with a small amount of viable tumor (blue) on either side of the non-viable region.

Table 2 shows average MRI parameter values in the entire center slice, consisting of both HIFU-treated and non-treated tumor

Table 2. MR parameter values (mean ± SD) in the entire center tumor slice of the HIFU-treated rats before HIFU, directly after HIFU, and 3 days after HIFU, as well as in the control animals on day 0 and day 3. For the HIFU-treated animals, the p values next to the average endogenous parameter values (T_1, T_2, ADC, APTw signal and $T_{1\rho}$) result from a paired two-sided Student t-test between the 'directly after HIFU' ($n = 12$; * indicates a significant difference) or '3 days after HIFU' ($n = 6$, [#] indicates a significant difference) data and the data for the corresponding rats in the 'before HIFU' group. The p values next to the average pharmacokinetic parameter values (K^{trans} and v_e) result from a two-sided Student t-test between the HIFU-treated and non-treated control tumors at the corresponding time points, either day 0 ([&] indicates a significant difference) or 3 ([$] indicates a significant difference). The p values given for the control animals on day 3 result from a two-sided paired Student t-test ($P < 0.05$) between the data on day 0 and day 3. The p values are highlighted bold if the mean MR parameter values showed statistically significant differences ($P < 0.05$). 'n.a.' indicates that these parameters were not measured before HIFU treatment

| Parameter | HIFU-treated animals | | | Control animals | |
	Before HIFU	Directly after HIFU	3 days after HIFU	Day 0	Day 3
T_1 [ms]	1674±41	1694±57; P=0.085	1520±134; **P=0.041** [#]	1624±63	1581±96; P=0.347
T_2 [ms]	183±16	173±29; P=0.152	160±17; P=0.111	198±45	177±39; P=0.423
ADC [10^{-3} mm^2/s]	1.14±0.14	1.04±0.14; **P=0.030** *	1.65±0.17; **P=0.001** [#]	1.21±0.19	1.27±0.13; P=0.614
APTw signal [%]	2.23±0.71	2.39±0.66; P=0.538	1.55±1.36; P=0.150	2.67±0.86	2.63±1.25; P=0.925
$T_{1\rho}$ B$_1$=350 Hz [ms]	127±9	136±18; P=0.178	119±15; P=0.604	116±20	115±22; P=0.918
K^{trans} [min^{-1}]	n.a.	0.013±0.010 **P=0.013** [&]	0.044±0.013 **P=0.048** [$]	0.076±0.034	0.085±0.041; P=0.560
v_e [—]	n.a.	0.093±0.046 **P=0.000** [&]	0.205±0.068 P=0.095	0.258±0.040	0.332±0.151; P=0.301

tissue because of the partial tumor ablation. HIFU treatment resulted in a subtle, yet significant, decrease in ADC directly after HIFU, whereas ADC values were pronouncedly, and significantly, increased 3 days after HIFU. In addition, T_1 values were significantly decreased 3 days after HIFU compared with before HIFU. The K^{trans} and v_e values were significantly lower in the HIFU-treated tumors directly after HIFU compared with the control tumors on day 0. At 3 days after HIFU treatment, K^{trans} remained significantly lower in the HIFU-treated tumors compared with the control tumors.

Further insight into the MR parameter distributions in the tumor tissue at the different experimental time points is provided by the histograms of MR parameter values in all tumor pixels in the center slice, which can be found in the Supplementary Information (Supplementary Information 3). The most notable changes in these histograms were observed 3 days after HIFU treatment. At that time point, a pronounced significant shift toward high ADC values and a slight, non-significant, shift toward low APT-weighted signal values were observed. Results of the analysis of the relation between temperature/thermal dose and changes in MR parameter values directly after treatment can also be found in the Supplementary Information (Supplementary Information 4).

Cluster analysis and feature vector selection

After evaluation of the changes in the individual MR parameters, cluster analysis was performed to combine information of the different endogenous contrast MR parameters to identify HIFU-treated non-viable tumor tissue. Clusters were classified as non-viable when the fraction of pixels within the clusters significantly increased after HIFU treatment. Subsequently, the one-to-one correspondence ($R^2_{y=x}$) between the non-viable tumor fractions derived from clustering with all different feature vectors and the histology-derived non-viable tumor fractions was determined. All experimental groups were included in this analysis. Clustering with four clusters led to a stronger one-to-one correspondence between histology and clustering compared with other numbers of clusters. $R^2_{y=x}$ values between histology-derived non-viable tumor fractions and non-viable tumor fractions derived from clustering with four clusters are displayed in Table 3 for all feature vectors. Feature vector {ADC, APTw signal} was identified as the optimal feature vector, since clustering with these two MR parameters resulted in the best one-to-one correspondence ($R^2_{y=x} = 0.92$) between the histology-derived and clustering-derived non-viable tumor fractions.

Representative cluster maps, resulting from clustering with the optimal feature vector {ADC, APTw signal} and four clusters, for all rats that underwent MRI follow-up until 3 days after MR–HIFU are shown in Fig. 2 at the three experimental time points. Before HIFU, almost all tumor pixels were assigned to the cyan and blue clusters. Also directly after HIFU treatment, only a minor number of pixels were assigned to the yellow and orange clusters. However, 3 days after HIFU treatment large regions emerged in which pixels were assigned to the yellow and orange clusters. Remarkably, in Rat 3 most tumor pixels remained in the blue and cyan clusters 3 days after treatment, indicative of the presence of a substantial amount of residual viable tumor tissue, which was confirmed by histology (see later in this section). However, the MR thermometry measurements suggested a successful ablation of this particular tumor (maximum temperature = 65.3 °C, 240 CEM fraction = 0.32).

Table 3. One-to-one correspondence ($R^2_{y=x}$) between histology-derived non-viable tumor fractions and non-viable tumor fractions resulting from k-means clustering with four clusters and all possible feature vectors (i.e. combinations of MR parameters). All groups ('directly after HIFU', '3 days after HIFU' and 'control') were combined in this analysis. The $R^2_{y=x}$ values are given for all feature vectors, grouped per number of MR parameters of which the feature vector consisted, and ordered from low to high values. The highest $R^2_{y=x}$ value is highlighted in bold (for feature vector {ADC, APTw signal})

	Feature vector	$R^2_{y=x}$
One parameter	$\{T_{1\rho}\}$	−21.7
	$\{T_2\}$	0.00
	{APTw signal}	0.00
	$\{T_1\}$	0.16
	{ADC}	0.63
Two parameters	$\{T_2,$ APTw signal$\}$	0.00
	$\{T_2, T_{1\rho}\}$	0.00
	{APTw signal, $T_{1\rho}\}$	0.23
	$\{T_1,$ ADC$\}$	0.29
	$\{T_1,$ APT$\}$	0.37
	$\{T_1, T_{1\rho}\}$	0.48
	$\{T_1, T_2\}$	0.58
	{ADC, $T_{1\rho}\}$	0.60
	$\{T_2,$ ADC$\}$	0.81
	{ADC, APTw signal}	**0.92**
Three parameters	$\{T_1, T_2, T_{1\rho}\}$	0.50
	$\{T_1,$ APTw signal, $T_{1\rho}\}$	0.51
	$\{T_2,$ APTw signal, $T_{1\rho}\}$	0.59
	$\{T_1, T_2,$ APTw signal$\}$	0.61
	$\{T_2,$ ADC, $T_{1\rho}\}$	0.61
	$\{T_1, T_2,$ ADC$\}$	0.68
	$\{T_1,$ ADC, $T_{1\rho}\}$	0.71
	$\{T_2,$ ADC, APTw signal$\}$	0.72
	{ADC, APTw signal, $T_{1\rho}\}$	0.73
	$\{T_1,$ ADC, APTw signal$\}$	0.74
Four parameters	$\{T_1, T_2,$ ADC, $T_{1\rho}\}$	0.55
	$\{T_1, T_2,$ APTw signal, $T_{1\rho}\}$	0.55
	$\{T_2,$ ADC, APTw signal, $T_{1\rho}\}$	0.74
	$\{T_1, T_2,$ ADC, APTw signal$\}$	0.86
	$\{T_1,$ ADC, APTw signal, $T_{1\rho}\}$	0.91
Five parameters	$\{T_1, T_2,$ ADC, APTw signal, $T_{1\rho}\}$	0.77

The fractions of pixels assigned to the different clusters following from segmentation with feature vector {ADC, APTw signal} at the three time points of the HIFU-treated animals are shown in Fig. 3. Indeed, a significantly increased fraction of pixels in the yellow and orange clusters was observed 3 days after HIFU compared with before treatment. These clusters were therefore classified as non-viable.

The average MR parameter values in the clusters resulting from segmentation with the optimal feature vector {ADC, APTw signal} are listed in Table 4. The clusters that were classified as non-viable were characterized by a high ADC value and either a low APT-weighted signal (yellow cluster) or an APT-weighted signal that is comparable to values measured before HIFU (orange cluster).

The qualitative visual agreement between the clustering-derived and histology-derived non-viable tumor tissue 3 days
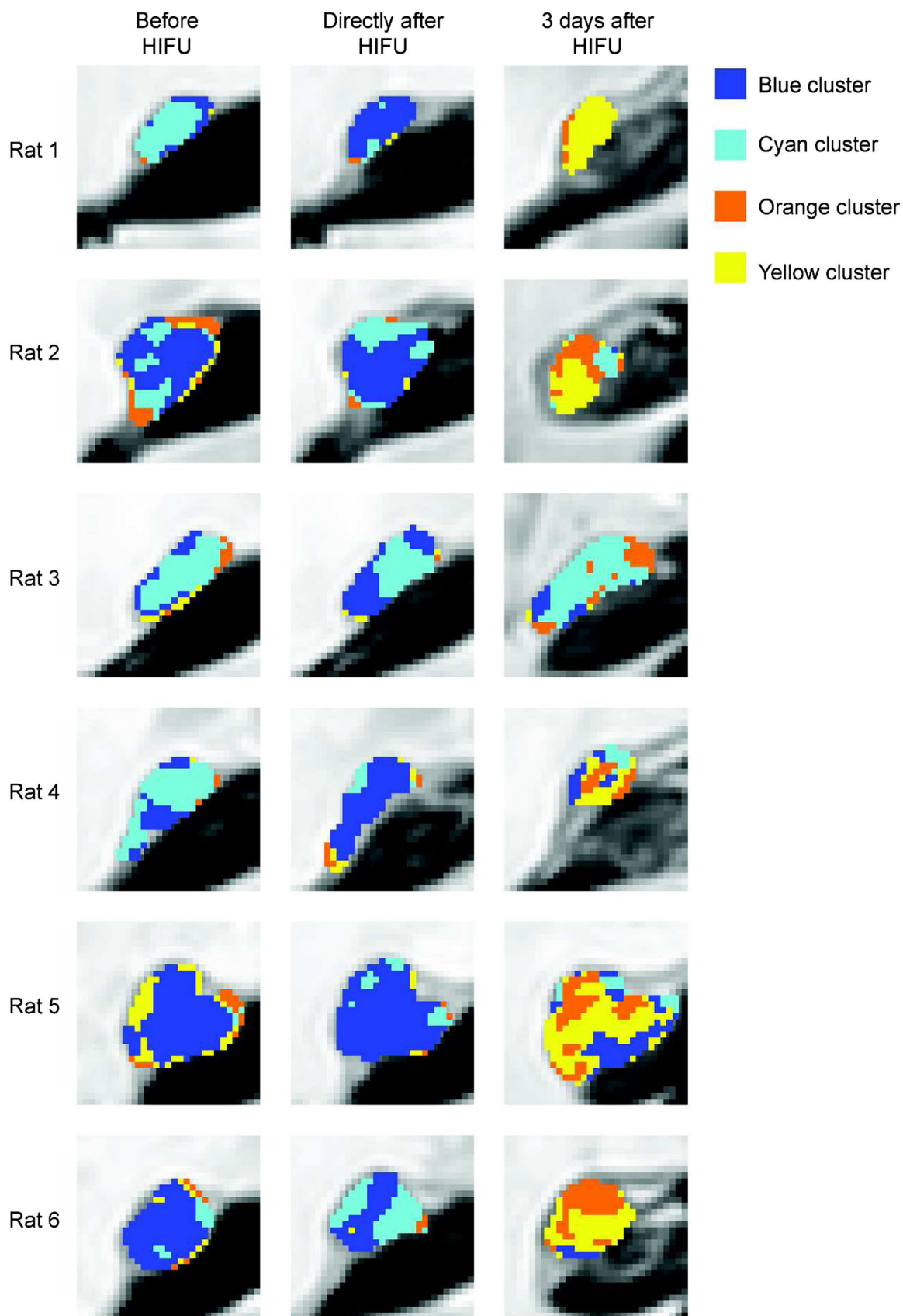
Figure 2. Representative results of *k*-means clustering with feature vector {ADC, APTw signal} and four clusters at the different experimental time points of all animals in the '3 days after HIFU' experimental group, superimposed on the tumor pixels in the T_2-weighted images. The MR slice of Rat 1 is the same as the slice shown in Figure 1. The four colors (cyan, blue, orange and yellow) indicate to which of the four clusters the tumor pixels were assigned.
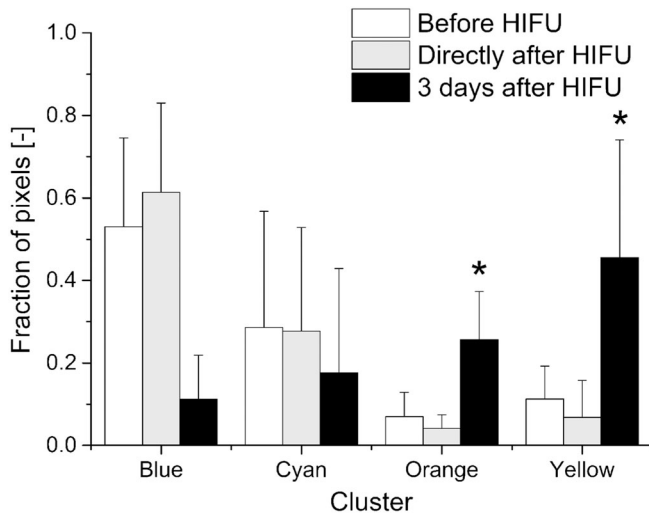
Figure 3. Bar chart of the fraction of pixels within the different clusters at the different experimental time points. * denotes a significant increase in the fraction of pixels within the cluster compared with before HIFU (one-sided paired Student *t*-test, $P < 0.05$).

Table 4. MR parameter values (mean ± SD) in the different clusters resulting from *k*-means clustering with feature vector {ADC, APTw signal} and four clusters

Cluster	ADC $[10^{-3}\ mm^2\ s^{-1}]$	APTw signal [%]
Blue	0.97 ± 0.18	1.83 ± 0.62
Cyan	1.11 ± 0.26	3.69 ± 0.76
Orange	2.20 ± 0.36	2.24 ± 1.13
Yellow	1.52 ± 0.26	0.97 ± 0.95

after HIFU treatment is depicted in Fig. 4. Large tumor regions were classified as non-viable by the cluster analysis. These regions were generally in good visual agreement with areas of non-viable tumor tissue in histology. The remarkable cluster results of Rat 3, which showed that the major part of the tumor was classified as viable 3 days after treatment, in contrast to what would be expected from the lethal thermal dose maps, were supported by histology. The NADH diaphorase-stained tumor section of this rat also indicated that a large part of the tumor was still viable 3 days after HIFU. A similar figure of the visual agreement between clustering and histology for the animals sacrificed directly after treatment is given in the Supplementary Information (Fig. S5). The visual agreement between clustering and histology was substantially lower at this time point after treatment.

The correlation plot in Fig. 5(A) demonstrates that clustering with four clusters and the optimal feature vector {ADC, APTw signal} resulted in a strong correlation ($r = 0.92$) and good one-to-one correspondence ($R^2_{y=x} = 0.92$, corresponding to the value in Table 3) between clustering-derived and histology-derived non-viable tumor fractions, when all data points of all experimental groups were combined. Directly after HIFU treatment, the agreement with histology was less ($r = 0.63$, $R^2_{y=x} = 0.62$; Fig. 5(B)). Nevertheless, Fig. 5(C) demonstrates that there was a strong correlation ($r = 0.87$) and excellent one-to-one correspondence ($R^2_{y=x} = 0.97$) between clustering-derived and

histology-derived non-viable tumor fractions 3 days after HIFU treatment. For the control animals (Fig. 5(D)) the correlation with histology was strong ($r = 0.95$), although the clustering-derived non-viable tumor fractions were consistently higher than the histology-derived non-viable tumor fractions ($R^2_{y=x} = 0.67$).

Correlation between 240 CEM fractions, non-perfused tumor fractions and histology

In order to compare the performance of the proposed multiparametric analysis with conventionally used HIFU treatment monitoring and evaluation methods, a similar correlation analysis between 240 CEM fractions, non-perfused fractions, deduced from DCE-MRI, and histology-derived non-viable fractions was performed (Fig. 6). A trend ($P = 0.070$) toward a strong correlation between the 240 CEM fraction and the histology-derived non-viable tumor fraction directly after HIFU was observed (Fig. 6(A)). Directly after treatment, no relation was found between the non-perfused and histology-derived non-viable tumor fractions (Fig. 6(B)). The non-perfused tumor fractions were consistently larger than the histology-derived non-viable tumor fractions. 3 days after HIFU, a strong positive correlation ($r = 0.90$) between the non-perfused fraction and histology-derived non-viable fraction was observed, although the non-perfused tumor fraction was consistently lower than the histology-derived non-viable tumor fraction (Fig. 6(C)).

A summary of the results of the correlation analyses between the histology-derived non-viable fractions and the 240 CEM, non-perfused and clustering-derived non-viable tumor fractions is displayed in Table 5. This table further illustrates that only the clustering-derived non-viable fractions 3 days after HIFU had a significant correlation and good agreement with the histology-derived non-viable tumor fractions.

H&E histology

Representative microscopy images of H&E-stained sections of tumors excised directly and 3 days after HIFU are shown in Fig. 7. At both time points, extensive necrosis was observed throughout the tumor tissue. Other major morphological changes observed directly after HIFU treatment were dilated and coagulated blood vessels and the infiltration of immune cells. HIFU-induced tissue damage was more pronouncedly visible 3 days after treatment. At that time point, extensive inflammation was seen in areas around the central zone of coagulative necrosis. In addition, cell debris and hemorrhages were observed.

DISCUSSION

In the present study, a multiparametric analysis was employed to identify treated (non-viable) and residual non-treated tumor tissue after MR–HIFU treatment. Global analysis of the MRI parameter values in the tumor tissue in the central MRI slice showed that HIFU-induced changes in the MRI parameters were more pronounced 3 days after HIFU compared with directly after treatment (Table 2). For the individual MR parameters only a subtle, yet significant, change in the average ADC in the tumor was observed directly after HIFU treatment. The detected decrease in ADC may be caused by cytotoxic cell swelling (35,36). In contrast, a strong increase in ADC was observed 3 days after HIFU treatment. This more pronounced change is likely attributable to necrosis-induced cell shrinkage, increased cell membrane
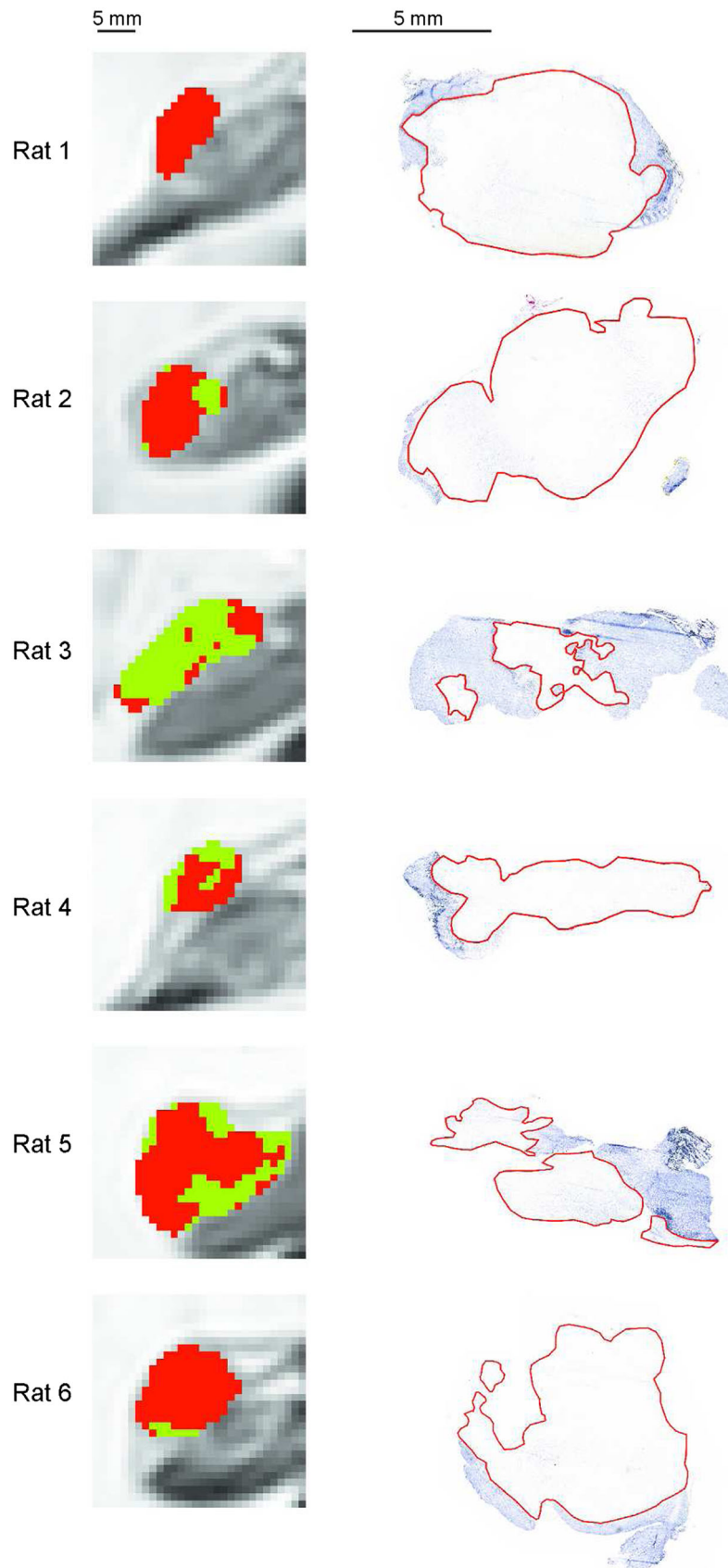
Figure 4. Classification of the tumor pixels as viable (green) or non-viable (red) from clustering with four clusters and feature vector {ADC, APTw signal} for all animals in the experimental group '3 days after HIFU', superimposed on the tumor pixels in the T_2-weighted images. The MR slice of Rat 1 is the same as the slice shown in Figure 1. On the right of the figure, the corresponding NADH diaphorase-stained tumor sections are shown. The tumor regions that were identified as non-viable on histology are delineated by red contours.
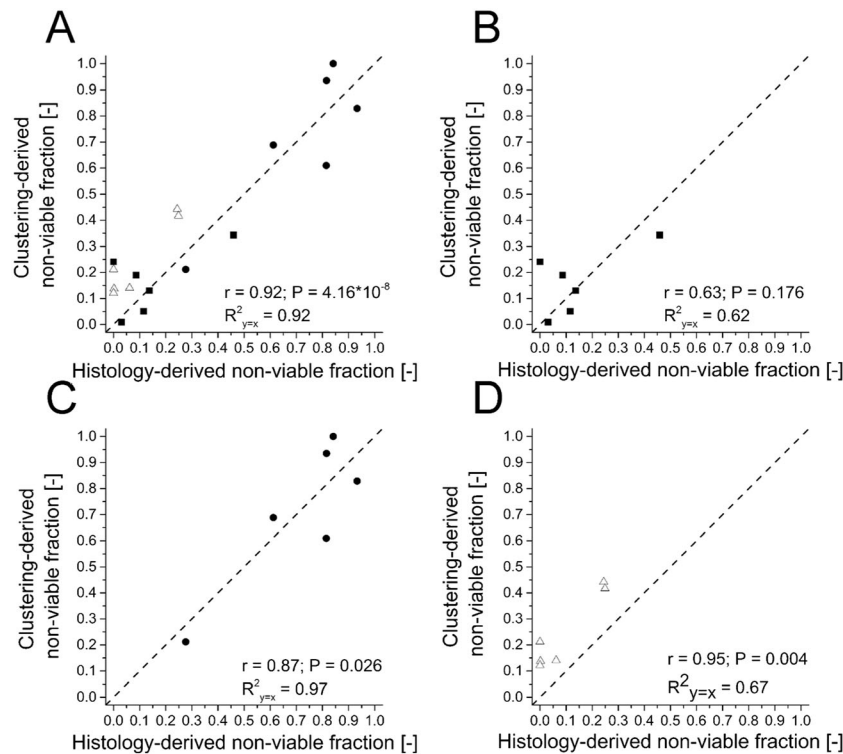
Figure 5. Correlation plots between clustering-derived and histology-derived non-viable tumor fractions resulting from *k*-means clustering with four clusters and feature vector {ADC, APTw signal}, for all data ('directly after HIFU', '3 days after HIFU' and 'control') (A) and for the individual experiment time points (B–D). The symbols ■, ● and Δ indicate the experimental groups 'directly after HIFU', '3 days after HIFU' and 'control', respectively. The dashed lines represent the line of identity *y* = *x*. Pearson's correlation coefficient with the corresponding *p* value and $R^2_{y=x}$ are listed in each correlation plot.

permeability and disruption of diffusion barriers in the necrotic tumor region (9,37). Related to this, the significant decrease in T_1 3 days after treatment was probably caused by an increased access of water molecules to paramagnetic sites and an increased macromolecular content in the interstitial space (37). Furthermore, a population of pixels with decreased APT-weighted signal intensity was identified in the APT parameter distribution 3 days after HIFU (Supplementary Information 3, Figure S3). This can be explained by protein aggregation due to thermal stress, which results in a decreased availability of mobile amide protons for exchange with the bulk water (21). In addition, changes in pH, for example due to ischemia, may have contributed to the decrease in APT-weighted signal (21). These above alterations in tumor morphology, to which the different MRI parameters are sensitive, apparently require time to develop and seem too subtle to allow for detection of endogenous MR contrast changes shortly after the thermal ablation. This was supported by the qualitative assessment of morphological changes after HIFU treatment with H&E staining (Fig. 7), which indicated that HIFU-induced tissue damage was more pronounced 3 days after treatment than directly after treatment.

The cluster analysis, in which multiple MRI parameters were combined in a single analysis, also showed the overall highest sensitivity for HIFU-induced cell death 3 days after treatment. At this time point, a strong correlation and high one-to-one correspondence was observed between histology-derived non-viable tumor fractions and non-viable tumor fractions derived from clustering with four clusters and feature vector {ADC, APTw signal}. The clustering-derived non-viable tumor fractions were determined by classification of clusters as non-viable if the fraction of pixels within the cluster significantly increased by HIFU treatment. For

some of the evaluated feature vectors, this criterion could however also be met if the cluster is associated with non-lethal HIFU-induced tissue changes. Nevertheless, because of the strong correlation between clustering-derived and histology-derived non-viable tumor fractions observed for feature vector {ADC, APTw signal}, it seems fair to assume that the non-viable clusters indeed represent non-viable tumor tissue for this particular feature vector.

In our previous study on multiparametric MRI analysis of HIFU-treated tumor tissue, we also found the largest correlation between MRI and histology 3 days after treatment. In that particular study, {T_1, T_2, ADC} was identified as the optimal feature vector for the identification of HIFU-treated, non-viable tumor tissue (13). In the current study it was hypothesized that addition of the advanced MRI parameters APT-weighted signal and $T_{1\rho}$ to the multiparametric MR analysis would improve its efficacy for early HIFU treatment evaluation, because these advanced MRI methods are expected to be sensitive to early HIFU treatment effects including protein denaturation. However, even with inclusion of these advanced parameters, the overall correlation between clustering and histology was lower directly after MR–HIFU ablation than 3 days after treatment. Directly after HIFU treatment, the highest one-to-one correspondence between clustering-derived and histology-derived non-viable fractions was observed for feature vector {T_1, $T_{1\rho}$}. At this time point, the $R^2_{y=x}$ value was 0.63 for this particular feature vector, which was substantially lower than the $R^2_{y=x}$ value of the feature vector that was identified as optimal ({ADC, APTw signal}) 3 days after treatment ($R^2_{y=x}$ = 0.97; Fig. 5(C)). Nevertheless, the APT-weighted signal appeared to be a valuable addition to the multiparametric analysis. In contrast to our previous study, in which three MRI
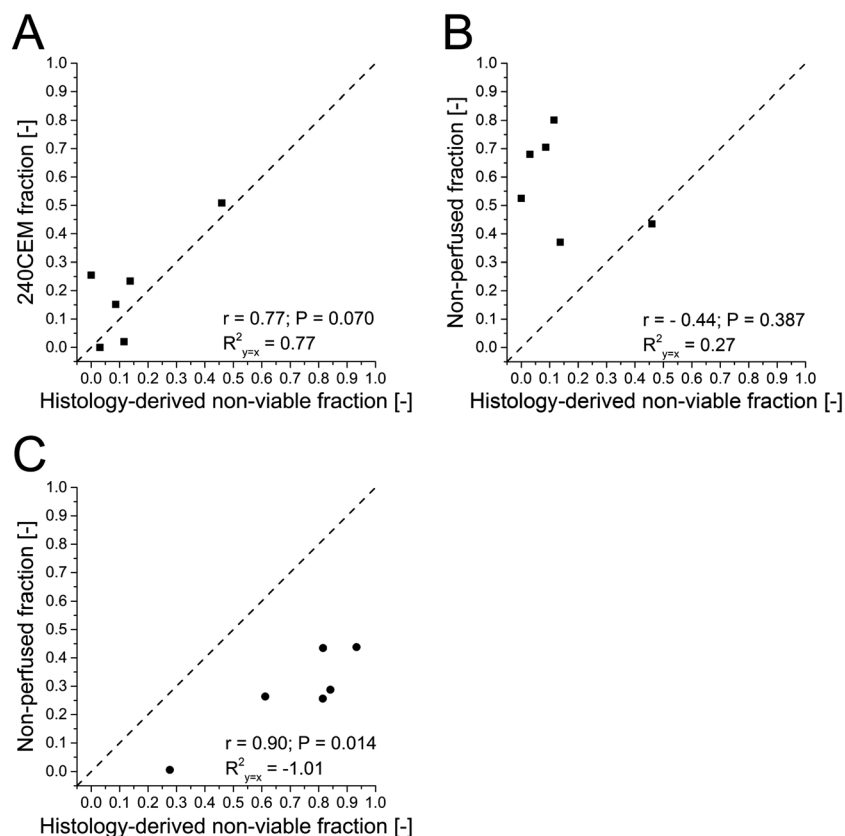
Figure 6. Correlation plots between the 240 CEM fractions and histology-derived non-viable fractions (A), non-perfused fractions and histology-derived non-viable fractions directly after HIFU (B) and non-perfused fractions and histology-derived non-viable fractions 3 days after HIFU (C). The symbols ■ and ● represent the experimental groups 'directly after HIFU' (A, B) and '3 days after HIFU' (C), respectively. The dashed line represents the line of identity $y = x$. Pearson's correlation coefficient with the corresponding p value and $R^2_{y=x}$ are listed in each correlation plot.

parameters were needed for the accurate identification of non-viable tumor tissue 3 days after treatment (13), in the current study the combined ADC and the APT data were sufficient to obtain an excellent agreement between the extent of non-viable tumor tissue identified by clustering and histology.

Importantly, measurement of a single endogenous contrast MRI parameter appeared to be unsuitable for accurate identification of HIFU-treated tumor tissue. No clear demarcation of the HIFU-treated tumor region could be observed in the different MR parameter maps (Fig. 1). In addition, the one-to-one correspondence between clustering-derived and histology-derived non-viable tumor fractions was low for all feature vectors consisting of one single MRI parameter (Table 3), which strongly indicates the additional value of multiparametric analysis for the evaluation of HIFU treatment as compared with therapy assessment based on analysis of separate MR images.

Inclusion of the DCE-MRI data to the cluster analysis may increase its sensitivity to early HIFU treatment effects by measuring changes in tumor vascular status. A significant reduction in K^{trans} and v_e was observed in the HIFU-treated tumors

Table 5. Overview of the results of the correlation analysis between the histology-derived non-viable fractions and the 240 CEM, non-perfused and clustering-derived (feature vector {ADC, APTw signal} and four clusters) non-viable fractions. S and NS indicate whether there was a significant or non-significant correlation ($P < 0.05$), respectively. The symbols $>$, $<$, $\approx$ and $=$ indicate whether the fractions indicated in the corresponding row heading were generally larger, smaller, almost equal or equal compared with the histology-derived non-viable fractions. – indicates that the correlation analysis was not performed, because the fractions could not be compared between the day of HIFU treatment and 3 days after HIFU treatment due to tumor progression (see the discussion section)

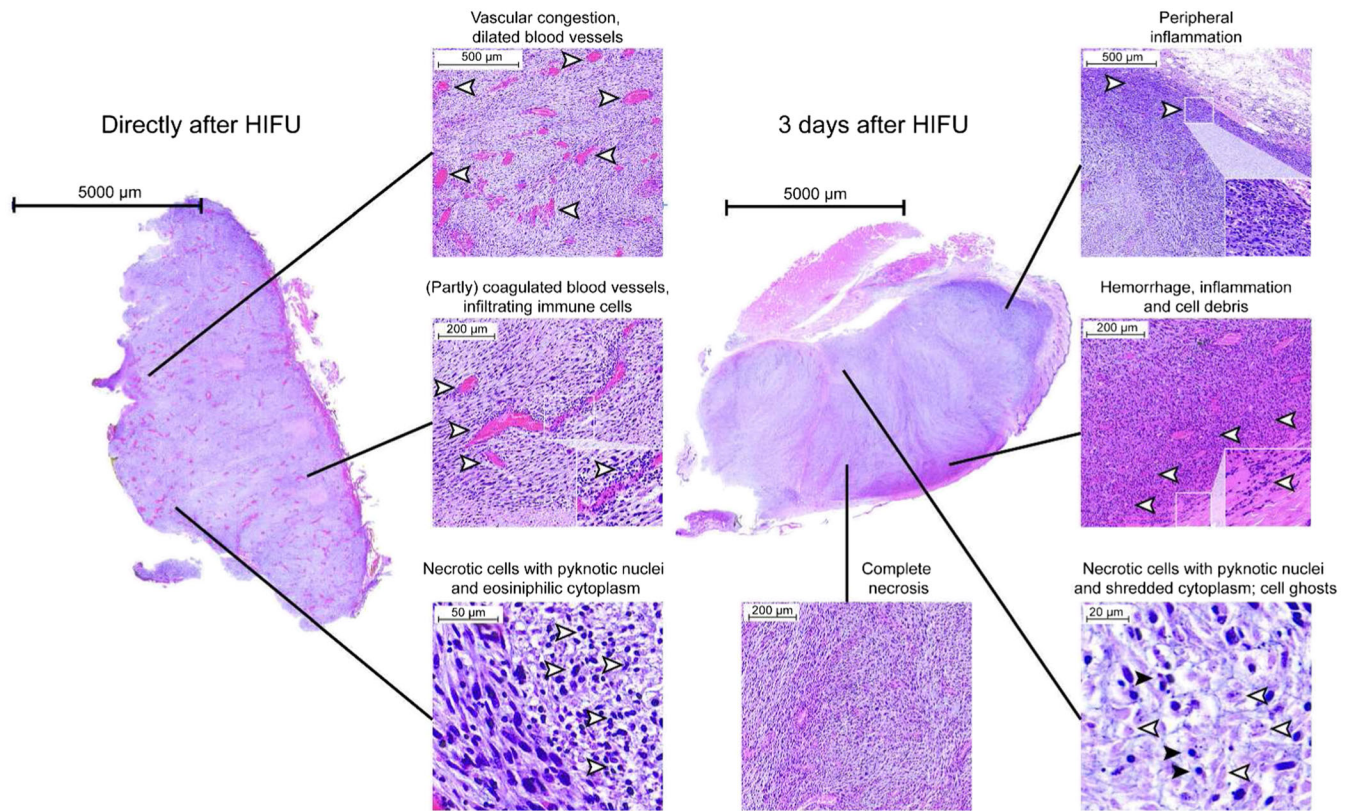|		Histology-derived non-viable fraction	
		Directly after	3 days after
240 CEM fraction		NS, $\approx$	–
Non-perfused fraction	Directly after	NS, $>$	–
	3 days after	–	S, $<$
Clustering-derived non-viable fraction	Directly after	NS, $\approx$	–
	3 days after	–	S, $=$

Figure 7. Representative brightfield microscopy images of H&E-stained sections of tumors excised directly (~2 h) and 3 days after treatment. Regions of specific interest are magnified and shown as separate images. The position of these regions within the tumor section is indicated with the black lines. The arrows in the images point to typical examples of the described features. The inset in the center right image of the tumor section obtained directly after HIFU shows a magnification of infiltrating immune cells. The inset in the top right image of the tumor section obtained 3 days after HIFU shows a magnification of the inflammatory cells. The hemorrhages and inflammation on the center right image of the tumor section obtained 3 days after HIFU were characterized by a red coloration and band of high cell density, respectively. The inset in this image shows a magnification of the cell debris. In the bottom right image of the tumor section obtained 3 days after HIFU, typical examples of the necrotic nuclei with pyknotic nuclei and shredded cytoplasm are indicated by the black arrows, whereas cell ghosts are indicated by the white arrows.

compared with control tumors. This decline in the DCE-MRI-derived pharmacokinetic parameters was probably caused by vascular destruction (38,39), which results in a lack of CA inflow in the treated tumor. However, although (D)CE-MRI may be more sensitive to HIFU-induced tissue changes directly after HIFU, the changes in contrast enhancement after HIFU treatment do not necessarily represent cell death. In fact, a poor agreement between non-perfused and histology-derived non-viable tumor fractions was observed both directly and 3 days after HIFU treatment. Directly after HIFU treatment, the non-perfused fraction was consistently larger than the non-viable fraction. This may be explained by the fact that HIFU-induced vascular destruction could extend beyond the central ablation zone, due to heat stress in regions surrounding this zone. It has been found in multiple studies that the non-perfused volume is generally larger than the estimated treatment volume (40–42) directly after HIFU thermal ablation. While coagulative necrosis is immediately induced in the central zone of ablation due to protein denaturation, cellular and nuclear membrane damage and halted metabolism (43), the vascular destruction in the peripheral zone may not directly result in tumor necrosis. Furthermore, temporary vascular occlusion (44) could have contributed to the relatively high non-perfused tumor fractions directly after HIFU. In contrast to directly after HIFU, 3 days after treatment the non-perfused tumor fraction was consistently lower than the non-viable

tumor fraction, which might be due to CA diffusion into the borders of the non-viable tumor area. A similar underestimation of the extent of non-viable tumor tissue by contrast-enhanced MRI has been reported in a study on HIFU treatment of rabbit tumors (45).

The 240 CEM thermal dose threshold can also not be regarded as suitable for predicting the extent of non-viable tissue after HIFU treatment. The thermal sensitivity varies widely between tissue types and therefore 240 CEM cannot be regarded as a universal threshold for lethal thermal dose (4,5). In the present study we observed a strong, but non-significant, correlation between histology-derived non-viable fractions and 240 CEM fractions (Fig. 6(A)). This correlation was higher than correlations between clustering-derived non-viable fractions based on any other single parameter and histology-derived non-viable fractions (Table 3), which would suggest that the 240 CEM threshold is promising for the detection of non-viable tumor tissue directly after HIFU. One should however take into account that HIFU-induced necrosis can extend beyond the thermal coagulation zone, because of delayed cell death due to vascular damage. Identification of non-viable tumor tissue after HIFU treatment solely based on the 240 CEM fraction would therefore likely underestimate the total extent of HIFU-induced cell death. An underestimation of the extent of tumor necrosis by the 240 CEM fraction was also reported in a pre-clinical study of HIFU-treated rabbit tumors (45).

A limitation of the current study is the lack of spatial registration between the subsequent MRI examinations of the same animal. Repositioning the tumor-bearing paw in exactly the same position as during the first MRI examination was practically impossible, mainly due to tumor progression between the examinations. Hence, quantitative analysis between MRI findings directly and 3 days after HIFU treatment was mainly restricted to global analysis of MRI parameter changes across the entire tumor. The effect of HIFU treatment on the MRI parameters is likely underestimated in this global analysis of average tumor parameter values, since both successfully treated and non-treated tumor tissue were included because of the partial tumor treatment. For the same reason, the 240 CEM, non-perfused and clustering-derived and histology-derived non-viable tumor fractions could not be quantitatively compared between the day of HIFU treatment and 3 days after HIFU treatment, because changes in fractions between these time points are influenced not only by the treatment, but also by tumor growth and slight differences in animal positioning. Potential follow-up studies on multiparametric MR evaluation of HIFU treatment could focus on the spatial registration between subsequent MRI examinations. This would require a set-up in which animals could be positioned repetitively in exactly the same orientation. In addition, a more slowly growing tumor model should be used to minimize tumor progression between subsequent time points. In such an ideal setting, the potential predictive value of the MRI measurements obtained directly after HIFU treatment on the extent of non-viable tumor tissue at later time points after treatment could be assessed. Another limitation of the study is the relatively small sample size for the different experimental groups. Therefore, in order to improve the statistical power, the optimal feature vector was selected based on the entire cohort of animals ($n = 18$) rather than on the different groups separately.

Although the best effort was made to match the cutting plane of histology with the center MRI slice, tissue deformation during histological processing is inevitable and therefore exact spatial registration between MRI and histology remained difficult. Consequently, the correlation analyses were based on tumor fractions rather than on absolute tumor areas. Furthermore, one should take into account that the thickness of the histological sections (5–6 μm) was substantially smaller than the MR slice thickness (2 mm), which can further explain deviations in the appearance of the tumor on MRI and in histology. For clinical application of the proposed multiparametric analysis a reduction of scan time of the multiparametric protocol may be necessary. The total acquisition time of the ADC and APT measurements was approximately 27 min. The scan time could possibly be shortened, without affecting accuracy, by decreasing the number of b values and irradiation offsets in the ADC and APT measurements, respectively. In addition, acceleration techniques such as parallel imaging (46,47) and compressed sensing (48) could be employed.

In the current study, we particularly chose the time point 3 days after HIFU treatment, because it has been shown in rabbit tumors that the ablation region increases in size for the first 3 days after HIFU treatment, after which it decreases again (45). Nevertheless, in follow-up studies on multiparametric MRI for evaluation of HIFU treatment it would be interesting to assess whether the proposed multiparametric analysis is also suitable for the assessment of the extent of non-viable tumor tissue at later stages of HIFU treatment. At these later stages, repair processes for example could influence the MRI parameter values (49).

In the current study an unsupervised clustering method was used for the segmentation of non-viable tumor tissue after HIFU treatment. While this clustering algorithm is particularly useful for data of groups of subjects, a supervised segmentation method may be more suitable for the segmentation of data of a single subject, as in clinical studies. Supervised segmentation algorithms, such as support vector machines, are regularly employed in MRI tumor segmentation studies (50) and may also be used in clinical studies on multiparametric MRI assessment of HIFU treatment.

In summary, we have demonstrated that a multiparametric MR analysis, especially based on ADC and the APT-weighted signal, can potentially be used to determine the extent of non-viable tumor tissue 3 days after HIFU treatment. The presented analysis outperformed the conventional methods that are used for monitoring and evaluation of HIFU therapy, i.e. thermal dose mapping and CE-MRI, respectively, with respect to the identification of non-viable tissue after treatment. Extensive validation of the proposed multiparametric analysis should be performed in different human tumor types to determine whether the observed changes in the ADC and APT-weighted signal are similar amongst tumors. We expect that, after this clinical validation, the proposed method can be incorporated in the current clinical workflow of MR–HIFU therapies.

Acknowledgements

REFERENCES

1. Kennedy JE. High-intensity focused ultrasound in the treatment of solid tumours. Nat. Rev. Cancer 2005; 5: 321–327.
2. ter Haar G. Therapeutic applications of ultrasound. Prog. Biophys. Mol. Biol. 2007; 93: 111–129.
3. de Senneville BD, Mougenot C, Quesson B, Dragonu I, Grenier N, Moonen CT. MR thermometry for monitoring tumor ablation. Eur. Radiol. 2007; 17: 2401–2410.
4. Yarmolenko PS, Moon EJ, Landon C, Manzoor A, Hochman DW, Viglianti BL, Dewhirst MW. Thresholds for thermal damage to normal tissues: an update. Int. J. Hyperthermia 2011; 27(4): 320–343.
5. Dewhirst MW, Viglianti BL, Lora-Michiels M, Hanson M, Hoopes PJ. Basic principles of thermal dosimetry and thermal thresholds for tissue damage from hyperthermia. Int. J. Hyperthermia 2003; 19(3): 267–294.
6. Zhou YF. High intensity focused ultrasound in clinical tumor ablation. World J. Clin. Oncol. 2011; 2: 8–27.
7. Venkatesan AM, Partanen A, Pulanic TK, Dreher MR, Fischer J, Zurawin RK, Muthupillai R, Sokka S, Nieminen HJ, Sinaii N, Merino M, Wood BJ, Stratton P. Magnetic resonance imaging-guided volumetric ablation of symptomatic leiomyomata: correlation of imaging with histology. J. Vasc. Interv. Radiol. 2012; 23: 786–794.e4.
8. Kim YS, Lim HK, Kim JH, Rhim H, Park BK, Keserci B, Kohler MO, Bae DS, Kim BG, Lee JW, Kim TJ, Sokka S, Lee JH. Dynamic contrast-enhanced magnetic resonance imaging predicts immediate therapeutic response of magnetic resonance-guided high-intensity focused ultrasound ablation of symptomatic uterine fibroids. Invest. Radiol. 2011; 46: 639–647.
9. Zhang Y, Zhao J, Guo D, Zhong W, Ran L. Evaluation of short-term response of high intensity focused ultrasound ablation for primary hepatic carcinoma: utility of contrast-enhanced MRI and diffusion-weighted imaging. Eur. J. Radiol. 2011; 79(3): 347–352.

10. Rouviere O, Girouin N, Glas L, Ben Cheikh A, Gelet A, Mege-Lechevallier F, Rabilloud M, Chapelon JY, Lyonnet D. Prostate cancer transrectal HIFU ablation: detection of local recurrences using T2-weighted and dynamic contrast-enhanced MRI. Eur. Radiol. 2010; 20: 48–55.

11. Kirkham AP, Emberton M, Hoh IM, Illing RO, Freeman AA, Allen C. MR imaging of prostate after treatment with high-intensity focused ultrasound. Radiology 2008; 246: 833–844.

12. Sung HY, Jung SE, Cho SH, Zhou K, Han JY, Han ST, Kim JI, Kim JK, Choi JY, Yoon SK, Yang JM, Han CW, Lee YS. Long-term outcome of high-intensity focused ultrasound in advanced pancreatic cancer. Pancreas 2011; 40(7): 1080–1086.

13. Hectors SJ, Jacobs I, Strijkers GJ, Nicolay K. Multiparametric MRI analysis for the identification of high intensity focused ultrasound-treated tumor tissue. PLoS One 2014a; 9: e99936.

14. Zhou J, Lal B, Wilson DA, Laterra J, van Zijl PC. Amide proton transfer (APT) contrast for imaging of brain tumors. Magn. Reson. Med. 2003; 50: 1120–1126.

15. Salhotra A, Lal B, Laterra J, Sun PZ, van Zijl PC, Zhou J. Amide proton transfer imaging of 9L gliosarcoma and human glioblastoma xenografts. NMR Biomed. 2008; 21: 489–497.

16. Jones CK, Schlosser MJ, van Zijl PC, Pomper MG, Golay X, Zhou J. Amide proton transfer imaging of human brain tumors at 3T. Magn. Reson. Med. 2006; 56: 585–592.

17. Zhou J, Blakeley JO, Hua J, Kim M, Laterra J, Pomper MG, van Zijl PC. Practical data acquisition method for human brain tumor amide proton transfer (APT) imaging. Magn. Reson. Med. 2008; 60: 842–849.

18. Dula AN, Arlinghaus LR, Dortch RD, Dewey BE, Whisenant JG, Ayers GD, Yankeelov TE, Smith SA. Amide proton transfer imaging of the breast at 3 T: establishing reproducibility and possible feasibility assessing chemotherapy response. Magn. Reson. Med. 2013; 70: 216–224.

19. Jia G, Abaza R, Williams JD, Zynger DL, Zhou J, Shah ZK, Patel M, Sammet S, Wei L, Bahnson RR, Knopp MV. Amide proton transfer MR imaging of prostate cancer: a preliminary study. J. Magn. Reson. Imaging 2011; 33: 647–654.

20. Zhou J, Tryggestad E, Wen Z, Lal B, Zhou T, Grossman R, Wang S, Yan K, Fu D, Ford E, Tyler B, Blakeley JO, Laterra J, Van Zijl P. Differentiation between glioma and radiation necrosis using molecular magnetic resonance imaging of endogenous proteins and peptides. Nat. Med. 2011; 17: 130–134.

21. Hectors SJ, Jacobs I, Strijkers GJ, Nicolay K. Amide proton transfer imaging of high intensity focused ultrasound-treated tumor tissue. Magn. Reson. Med. 2014; 72: 1113–1122.

22. Hectors SJ, Moonen RP, Strijkers GJ, Nicolay K. $T_{1\rho}$ mapping for the evaluation of high intensity focused ultrasound tumor treatment. Magn. Reson. Med. 2015 Apr; 73(4): 1593–1601.

23. Hijnen NM, Heijman E, Kohler MO, Ylihautala M, Ehnholm GJ, Simonetti AW, Grull H. Tumour hyperthermia and ablation in rats using a clinical MR–HIFU system equipped with a dedicated small animal set-up. Int. J. Hyperthermia 2012; 28: 141–155.

24. Kohler MO, Mougenot C, Quesson B, Enholm J, Le Bail B, Laurent C, Moonen CT, Ehnholm GJ. Volumetric HIFU ablation under 3D guidance of rapid MRI thermometry. Med. Phys. 2009; 36: 3521–3535.

25. Köhler MO, Enholm J, Mougenot C, Andreae T. Sonalleve MR–HIFU – Philips MR-Guided High Intensity Focused Ultrasound. 2011. http://www.healthcare.philips.com/pwc_hc/ru_ru/about/Events/RSNA/pdfs/MR_Sonalleve_HIFU_whitepaper.pdf [29 August 2014].

26. Hijnen NM, Elevelt A, Grüll H. Stability and trapping of magnetic resonance imaging contrast agents during high-intensity focused ultrasound ablation therapy. Invest. Radiol. 2013; 48: 517–524.

27. Deichmann R, Haase A. Quantification of T1 values by SNAPSHOT-FLASH NMR imaging. J. Magn. Reson. 1992; 96: 608–612.

28. Deoni SC, Rutt BK, Peters TM. Rapid combined T_1 and T_2 mapping using gradient recalled acquisition in the steady state. Magn. Reson. Med. 2003; 49(3): 515–526.

29. Tofts PS, Brix G, Buckley DL, Evelhoch JL, Henderson E, Knopp MV, Larsson HB, Lee TY, Mayr NA, Parker GJ, Port RE, Taylor J, Weisskoff RM. Estimating kinetic parameters from dynamic contrast-enhanced T_1-weighted MRI of a diffusable tracer: standardized quantities and symbols. J. Magn. Reson. Imaging 1999; 10: 223–232.

30. McGrath DM, Bradley DP, Tessier JL, Lacey T, Taylor CJ, Parker GJ. Comparison of model-based arterial input functions for dynamic contrast-enhanced MRI in tumor bearing rats. Magn. Reson. Med. 2009; 61(5): 1173–1184.

31. Charles River Laboratories. Rat Hematology Data Sheet. 2012. http://www.criver.com/files/pdfs/rms/fischer-cdf/rm_rm_r_cdf_fisher_rat_clinical_pathology_data.aspx [1 September 2014].

32. Sapareto SA, Dewey WC. Thermal dose determination in cancer therapy. Int. J. Radiat. Oncol. Biol. Phys. 1984; 10(6): 787–800.

33. Omran MGH, Engelbrecht AP, Salman A. An overview of clustering methods. Intell. Data Anal. 2007; 11: 583–605.

34. Chatterjee S, Hadi AS. *Regression Analysis by Example*. John Wlley & Sons, Inc.: Hoboken, New Jersey; 2006.

35. Jacobs MA, Ouwerkerk R, Kamel I, Bottomley PA, Bluemke DA, Kim HS. Proton, diffusion-weighted imaging, and sodium (23Na) MRI of uterine leiomyomata after MR-guided high-intensity focused ultrasound: a preliminary study. J. Magn. Reson. Imaging 2009; 29(3): 649–656.

36. Jacobs MA, Gultekin DH, Kim HS. Comparison between diffusion-weighted imaging, T2-weighted, and postcontrast T1-weighted imaging after MR-guided, high intensity, focused ultrasound treatment of uterine leiomyomata: preliminary results. Med. Phys. 2010; 37(9): 4768–4776.

37. Graham SJ, Stanisz GJ, Kecojevic A, Bronskill MJ, Henkelman RM. Analysis of changes in MR properties of tissues after heat treatment. Magn. Reson. Med. 1999; 42: 1061–1071.

38. Wu F, Chen WZ, Bai J, Zou JZ, Wang ZL, Zhu H, Wang ZB. Tumor vessel destruction resulting from high-intensity focused ultrasound in patients with solid malignancies. Ultrasound Med. Biol. 2002; 28: 535–542.

39. Cheng HL, Purcell CM, Bilbao JM, Plewes DB. Prediction of subtle thermal histopathological change using a novel analysis of Gd-DTPA kinetics. J. Magn. Reson. Imaging 2003; 18: 585–598.

40. Pilatou MC, Stewart EA, Maier SE, Fennessy FM, Hynynen K, Tempany CM, McDannold N. MRI-based thermal dosimetry and diffusion-weighted imaging of MRI-guided focused ultrasound thermal ablation of uterine fibroids. J. Magn. Reson. Imaging 2009; 29(2): 404–411.

41. Tempany CM, Stewart EA, McDannold N, Quade BJ, Jolesz FA, Hynynen K. MR imaging-guided focused ultrasound surgery of uterine leiomyomas: a feasibility study. Radiology 2003; 226(3): 897–905.

42. McDannold N, Tempany CM, Fennessy FM, So MJ, Rybicki FJ, Stewart EA, Jolesz FA, Hynynen K. Uterine leiomyomas: MR imaging-based thermometry and thermal dosimetry during focused ultrasound thermal ablation. Radiology 2006; 240: 263–272.

43. Chu KF, Dupuy DE. Thermal ablation of tumours: biological mechanisms and advances in therapy. Nat. Rev. Cancer 2014; 14: 199–208.

44. Hynynen K, Chung AH, Colucci V, Jolesz FA. Potential adverse effects of high-intensity focused ultrasound exposure on blood vessels *in vivo*. Ultrasound Med. Biol. 1996; 22: 193–201.

45. Wijlemans JW, Deckers R, van den Bosch MA, Seinstra BA, van Stralen M, van Diest PJ, Moonen CT, Bartels LW. evolution of the ablation region after magnetic resonance-guided high-intensity focused ultrasound ablation in a Vx2 tumor model. Invest. Radiol. 2013; 48: 381–386.

46. Pruessmann KP, Weiger M, Scheidegger MB, Boesiger P. SENSE: sensitivity encoding for fast MRI. Magn. Reson. Med. 1999; 42(5): 952–962.

47. Griswold MA, Jakob PM, Heidemann RM, Nittka M, Jellus V, Wang J, Kiefer B, Haase A. Generalized autocalibrating partially parallel acquisitions (GRAPPA). Magn. Reson. Med. 2002; 47(6): 1202–1210.

48. Geethanath S, Reddy R, Konar AS, Imam S, Sundaresan R, D RR, Venkatesan R. Compressed sensing MRI: a review. Crit. Rev. Biomed. Eng. 2013; 41(3): 183–204.

49. Cheng HL, Purcell CM, Bilbao JM, Plewes DB. Usefulness of contrast kinetics for predicting and monitoring tissue changes in muscle following thermal therapy in long survival studies. J. Magn. Reson. Imaging 2004; 19: 329–341.

50. Gordillo N, Montseny E, Sobrevilla P. State of the art survey on MRI brain tumor segmentation. Magn. Reson. Imaging 2013; 31(8): 1426–1438.

51. Witschey WR II, Borthakur A, Elliott MA, Mellon E, Niyogi S, Wallman DJ, Wang C, Reddy R. Artifacts in T1ρ-weighted imaging: compensation for B_1 and B_0 field imperfections. J. Magn. Reson. 2007; 186: 75–85.

SUPPORTING INFORMATION

Additional supporting information may be found in the online version of this article at the publisher's web site.